

Chaperone-mediated autophagy manipulates PGC1 α stability and governs energy metabolism under thermal stress

Received: 17 June 2024

Accepted: 29 April 2025

Published online: 14 May 2025



Yixiao Zhuang^{1,10}, Xinyi Zhang^{1,10}, Shuang Zhang^{1,10}, Yunpeng Sun^{2,10}, Hui Wang¹, Yuxuan Chen¹, Hanyin Zhang¹, Penglai Zou¹, Yonghao Feng¹, Xiaodan Lu³, Peijie Chen⁴, Yi Xu⁵, John Zhong Li^{6,7,8}, Huanqing Gao¹✉, Li Jin¹✉ & Xingxing Kong^{1,5,9}✉

Thermogenic proteins are down-regulated under thermal stress, including PGC1 α . However, the molecular mechanisms are not fully understood. Here, we addressed that chaperone-mediated autophagy could regulate the stability of PGC1 α under thermal stress. In mice, knockdown of Lamp2a, one of the two components of CMA, in BAT showed increased PGC1 α protein and improved metabolic phenotypes. Combining the proteomics of brown adipose tissue (BAT), structure prediction, co-immunoprecipitation- mass spectrum and biochemical assays, we found that PARK7, a Parkinson's disease causative protein, could sense the temperature changes and interact with LAMP2A and HSC70, respectively, subsequently manipulate the activity of CMA. Knockout of Park7 specific in BAT promoted BAT whitening, leading to impaired insulin sensitivity and energy expenditure at thermoneutrality. Moreover, inhibiting the activity of CMA by knockdown of LAMP2A reversed the effects induced by Park7 ablation. These findings suggest CMA is required for BAT to sustain thermoneutrality-induced whitening through degradation of PGC1 α .

Ambient temperature has a profound influence on body metabolism and energy expenditure, particularly affecting brown adipose tissue (BAT) morphology and biology¹. When exposed to cold, BAT can be activated to generate non-shivering thermogenesis via the inner mitochondrial membrane protein—uncoupling protein 1 (UCP1). This process significantly increases the overall energy expenditure of the body². However, humans spend the majority of their lives in thermoneutral conditions^{3,4}, where there is no need for BAT

recruitment or activity. For research purposes, thermoneutrality (TN) is considered the best housing temperature for mice to mimic human metabolism^{5,6}. In mice, and likely in humans as well, prolonged exposure to thermoneutral temperatures leads to BAT whitening, an involution process characterized by the accumulation of large unilocular lipid droplets, mitochondrial degeneration and dysfunction, and inflammation⁷. More specifically, the expressions of thermogenic genes, such as peroxisome proliferator-activated

¹State Key Laboratory of Genetic Engineering, School of Life Sciences, Fudan University, Shanghai 200438, China. ²Interdisciplinary Research Center on Biology and Chemistry, Shanghai Institute of Organic Chemistry, Chinese Academy of Sciences, Shanghai 201210, China. ³Precisional Medical Center, Jilin Province People's Hospital, Changchun 130021, China. ⁴School of Exercise and Health, Shanghai University of Sport, Shanghai 200438, China. ⁵Shanghai Key Laboratory of Metabolic Remodeling and Health, Institute of Metabolism and Integrative Biology, Fudan University, Shanghai 200438, China. ⁶Department of Molecular Biology and Biochemistry, Nanjing Medical University, Nanjing, Jiangsu 211166, China. ⁷Jiangsu Key Laboratory of Molecular Targets and Intervention of Metabolic Disease, Nanjing Medical University, Nanjing, Jiangsu 211166, China. ⁸Collaborative Innovation Center for Cardiovascular Disease Translational Medicine, Nanjing Medical University, Nanjing, Jiangsu 211166, China. ⁹Department of Endocrinology and Metabolism, Huashan Hospital, Fudan University, Shanghai 200438, China. ¹⁰These authors contributed equally: Yixiao Zhuang, Xinyi Zhang, Shuang Zhang, Yunpeng Sun.

✉ e-mail: gao_hq@fudan.edu.cn; lijin@fudan.edu.cn; kongxingxing@fudan.edu.cn

receptor gamma coactivator 1- α (PGC1 α) and UCP1, significantly decrease with warm acclimation⁸. However, the molecular mechanisms underlying the degradation of these proteins under thermal stress are not fully understood.

The transcriptional co-activator PGC1 α is a broad and powerful regulator of many metabolic processes in different tissues. The expression and activity of PGC1 α are controlled in dynamic state dictated by the balance of its synthesis and degradation. Indeed, misregulation of PGC1 α levels has been implicated in the pathogenesis of several diseases, including diabetes, obesity, heart diseases, and neurological disorders^{9,10}. We and some other groups have addressed determinants of PGC1 α synthesis^{11,12}. Though several groups indicated that PGC1 α is a substrate for degradation by the proteasome^{9,13,14}, there is relatively little understanding of other mechanism(s) and regulation of PGC1 α degradation.

Although it has been demonstrated that the temperature-induced whitening process in BAT depends on autophagy¹⁵, there is currently no direct evidence regarding which specific type of autophagy is involved in BAT whitening at TN. There are three types of autophagy: macro-autophagy, micro-autophagy, and chaperone-mediated autophagy (CMA). CMA is the only autophagy type that selectively degrades cellular proteins endowed with a KFERQ-like motif by lysosomes¹⁶. Mechanistically, the KFERQ-like motifs present in substrate proteins are recognized by the molecular chaperone heat shock cognate 71 kDa protein (HSC70), and directed to LAMP2A, which acts as the CMA receptor at the lysosomal surface. It is estimated that 30% of all cellular proteins can be directed to the lysosome for CMA degradation, but only a few substrates have been formally identified so far¹⁷. Although CMA can degrade key enzymes related to carbohydrate and lipid metabolism in the liver¹⁸, its role in adipose tissue biology is yet to be understood¹⁹. Besides, how the CMA is regulated under different conditions is not fully known.

The Park7 is responsible for causing autosomal recessive early-onset familial Parkinson's disease (PD)²⁰. The PD-associated loss of Park7 function is related to reduced lysosomal activity and mitochondrial damage in neuronal cells²¹. Furthermore, Park7 plays multiple roles in various metabolic cells. For example, in white adipocytes, silencing of Park7 in 3T3-L1 has been shown to reduce adipogenic differentiation and decrease the expression of markers associated with mature adipocytes²². Global knockout Park7 resulted in brown adipose tissue impairment in obesity mice, but the mechanism is not clear²³. In beta cells, Park7 protects cells from numerous cell stresses and preserves insulin secretion^{24–26}. Notably, Shi et al. demonstrated that mice lacking Park7 were leaner and had reduced inflammation²⁷. Conversely, another study by Kim et al. did not observe any changes in insulin resistance or glucose tolerance in the mice lacking Park7²². Given the difference between these two phenotypes, conditional knockout of Park7 would facilitate the elucidation of molecular mechanisms.

This study found that CMA is required for the degradation of PGC1 α under thermal stress. We identified a chaperone, PARK7, can interact with LAMP2A and HSC70, respectively, subsequently manipulate the activity of CMA adapt to temperature changes. In addition, knockdown of LAMP2A in BAT favored metabolic phenotypes, whereas the ablation of Park7 specific in BAT (Park7^{ΔUCP1}) was found to increase the activity of CMA, leading to the degradation of PGC1 α at thermoneutral conditions. Moreover, the results of reducing CMA activity by knocking down LAMP2A in BAT conflicted with the effects observed in Park7-defective mice. Despite the clinical potential of BAT-related treatments for obesity-associated metabolic diseases, thermoneutral adaptation causes BAT to lose its metabolic capacity and mitochondrial content. Thus, understanding the mechanism underlying BAT whitening may help identify pharmacological targets to preserve or regain BAT metabolic capacity in humans.

Results

Degradation of PGC1 α is induced by CMA under thermal stress

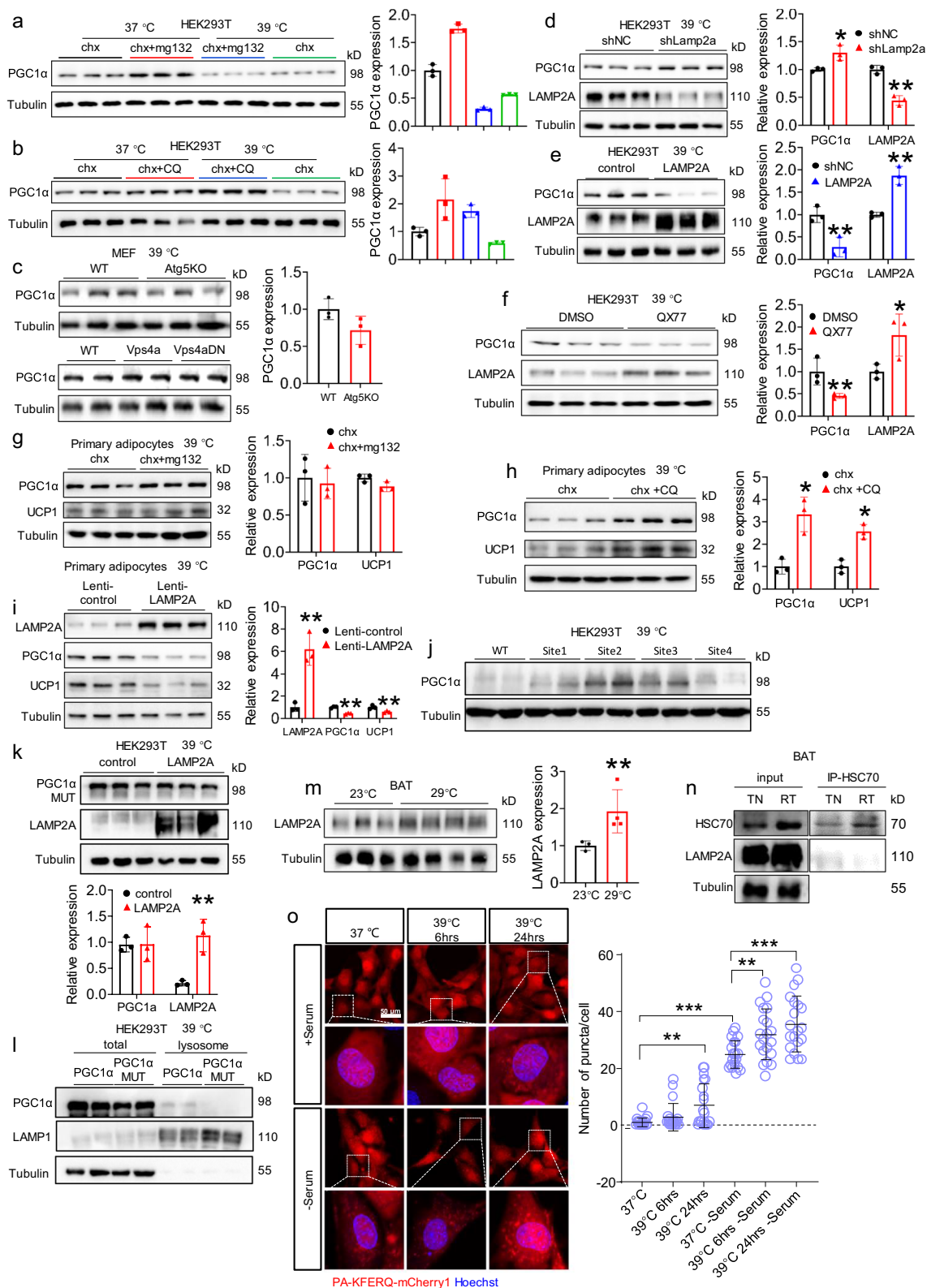
PGC1 α is a critical regulator of thermogenesis in highly oxidative tissues, which is greatly inducible by environmental stimuli such as cold. To investigate whether the stability of PGC1 α was affected by ubiquitination proteasome system under thermal stress, we treated cells with proteasome and calpain inhibitor and detect PGC1 α expression. We found that the degradation of PGC1 α was significantly inhibited by MG132, a potent proteasome and calpain inhibitor, at 37 °C when administered with cycloheximide (CHX), a protein synthesis inhibitor (Fig. 1a). However, MG132 could not efficiently inhibit the degradation at 39 °C (Fig. 1a), indicating that some other pathways contribute to the stability of PGC1 α under thermal stress. Autophagy-lysosome-based protein degradation is known to be a major quality control mechanism for cellular homeostasis²⁸. As a result, we treated the cells with an autophagy inhibitor, chloroquine (CQ). CHX was first added to the cells and PGC1 α was degraded with time, whereas CQ stabilized the protein levels of PGC1 α (Fig. 1b and Fig. S1a, b), demonstrating that autophagy contributed to the degradation of thermogenic proteins at TN²⁸. Subsequently, we explored the type of autophagy that is critical for the stability of thermogenic proteins under thermal exposure. While ATG5²⁹ and VPS4a³⁰ are required for the macro- and micro-autophagy, respectively, LAMP2A is essential for CMA activity. Although the protein levels of PGC1 α were not changed in ATG5KO or VPS4a overexpression or dominant negative cells (Fig. 1c), significant increases were observed in LAMP2A knockdown cells (Fig. 1d). Furthermore, LAMP2A overexpression downregulated PGC1 α protein levels (Fig. 1e). Consistent with this, PGC1 α was downregulated in cells treated with QX77, an enhancer of CMA activity (Fig. 1f).

BAT is known to be an important thermogenic tissue, whose activity is very sensitive to temperature¹. We thus confirmed the degradation of PGC1 α in primary brown adipocytes. As expected, inhibiting the activity of proteasome could not inhibit the degradation of PGC1 α at 39 °C (Fig. 1g), but the inhibition of autophagic activity enhanced the stability of PGC1 α (Fig. 1h). UCP1, a target of PGC1 α , was similarly changed to PGC1 α (Fig. 1g, h). Moreover, LAMP2A overexpression decreased the protein levels of PGC1 α and UCP1 in primary brown adipocytes (Fig. 1i).

CMA ensures the selective degradation of cellular proteins endowed with a KFERQ-like motif by lysosomes¹⁷. Using the KFERQ finder website to analyze the KFERQ-like motifs, three conserved motifs in PGC1 α were identified (Fig. S1c). We then generated mutants of PGC1 α (Fig. S1d) and compared their stability to those of the wild-type. The PGC1 α mutants (sites 1, 2 and 3) were more stable than the wild-type PGC1 α in HEK293T cells at 39 °C (Fig. 1j) or overexpressed LAMP2A (Fig. 1k). To confirm KFERQ-mutant PGC1 α is not degraded by lysosomes, we isolated the lysosomes and detected the PGC1 α level in the lysosome. As expected, KFERQ-mutant (3 sites) PGC1 α are not degraded by lysosomes (Fig. 1l). These findings suggested that CMA is important for the stability of PGC1 α under thermal stress. Additionally, the expression of LAMP2A was increased in BAT from mice housed at TN (Fig. 1m). The interaction between HSC70 and LAMP2A was enhanced under thermal stress (Fig. 1n). Consistent with this, the activity of CMA was induced by thermal stress (Fig. 1o), which may contribute to thermogenic protein degradation at TN.

Mice with BAT-specific Lamp2a knockdown show improved energy metabolism at TN

To further study the role of CMA in vivo, especially in response to thermogenic stimuli, we generated indicated mice models. Cuervo's group studied that CMA is important for adipogenesis by knocking out Lamp2a specifically in the fibro/adipogenic progenitor cells that give rise to white adipocytes¹⁹. Therefore, we directly injected the adeno-associated virus (AAV)-shLamp2a into BAT of 8-weeks aged mice to avoid the development of adipocytes. Four weeks after injection, the



protein level of LAMP2A was significantly decreased in BAT but not WAT (Fig. 2a). The body weight and body composition exhibited decreased compared with control mice housed at TN (Fig. 2b–d). The BAT mass was similar between two groups (Fig. 2e). The decreased body weight was not because of food intake, but increased energy expenditure, especially in dark cycle (Fig. 2f–i). Consistent with this, the insulin sensitivity was improved (Fig. 2j, k). Additionally, the size of

adipocytes was smaller (Fig. 2l) and the UCP1 staining was enhanced (Fig. 2m). We also measured the oxygen consumption of BAT. The maximum oxygen consumption rate (OCR) was enhanced (Fig. 2n). The protein levels of PGC1α and UCP1 were increased in the BAT with LAMP2A knockdown (Fig. 2o). These data suggested that mice with knockdown of LAMP2A in BAT show improved metabolic phenotypes compared to controls at TN.

Fig. 1 | Degradation of PGC1 α is induced by CMA under thermal stress.

a, b Immunoblotting for PGC1 α protein levels in HEK293T cells cultured in 37 °C or 39 °C for 24 h (representative of $n = 3$ independent experiments). **c** Immunoblotting for PGC1 α protein levels in MEF cells with/without ATG5 deletion or overexpressing VPS4A or VPS4A^{E228Q} (dominant negative) in 39 °C for 24 h and treated with 50 μ M cycloheximide (CHX) for 3 h before harvest cells (representative of $n = 3$ independent experiments). **d** Immunoblotting for PGC1 α and LAMP2A protein levels in HEK293T cells with/ without LAMP2A knockdown in 39 °C for 24 h and treated with 50 μ M cycloheximide (CHX) for 3 h before harvest cells (representative of $n = 3$ independent experiments). **e** Immunoblotting for PGC1 α and LAMP2A protein levels in HEK293T cells over-expressing LAMP2A in 39 °C for 24 h and treated with 50 μ M cycloheximide (CHX) for 3 h before harvest cells (representative of $n = 3$ independent experiments). **f** Immunoblotting for PGC1 α and LAMP2A protein levels in HEK293T cells treated with QX77 in 39 °C for 24 h and treated with 50 μ M cycloheximide (CHX) for 3 h before harvest cells (representative of $n = 3$ independent experiments). **g, h** Immunoblotting for PGC1 α and UCP1 protein levels in primary brown adipocytes in 39 °C for 24 h (representative of $n = 3$ independent experiments). **i** Immunoblotting for PGC1 α , UCP1 and LAMP2A protein levels in

primary brown adipocytes overexpressing LAMP2A in 39 °C for 24 h and treated with 50 μ M cycloheximide (CHX) for 3 h before harvest cells (representative of $n = 3$ independent experiments). **j** Immunoblotting for PGC1 α protein levels in HEK293T cells overexpressing PGC1 α wt/ mutants in 39 °C for 24 h and treated with 50 μ M cycloheximide (CHX) for 3 h before harvest cells (representative of $n = 3$ independent experiments). **k** Immunoblotting for PGC1 α and LAMP2A protein levels in HEK293T cells co-expressing LAMP2A and PGC1 α -MUT in 39 °C for 24 h and treated with 50 μ M cycloheximide (CHX) for 3 h before harvest cells (representative of $n = 3$ independent experiments). **l** Immunoblotting for PGC1 α protein levels in HEK293T cells overexpressing PGC1 α wt/ mutants in 39 °C for 24 h. **m** Endogenous Co-IP analysis of HSC70 and LAMP2A in BAT from mice housed at RT and TN ($n = 3$ mice for 23 °C group, $n = 4$ for 29 °C group). **n** Immunoblotting for LAMP2A protein level in BAT from mice housed at RT and TN. **o** Representative cell images and quantitation of CMA flux of NIH-3T3 cells expressing KFERQ-PA-mCherry1 ($n = 20$). Scale bar, 50 μ m. Statistical significance was assessed by unpaired Student's *t*-test. All results were expressed as means \pm SEM and $^{**}p < 0.01$, $^{***}p < 0.005$. Student's two-tailed unpaired *T*-test for 2-group comparisons. Source data are provided as a Source Data file.

PARK7 interacts with LAMP2A and regulates PGC1 α degradation

Next, we tried to figure out how CMA is regulated by different temperatures. We analyzed computational proteomics of BAT, combined with the STRING database, a protein-protein association network tool³¹, to perform structure prediction, along with immunoprecipitation-mass spectrometry (IP-MS) to identify the proteins interacting with LAMP2A (Fig. 3a). Firstly, we performed proteomics on BAT from mice housed at different temperatures (cold, 4 °C; room temperature, RT, 23 °C; TN, 29 °C) (Fig. 3b). Consistent with RNA-seq data from Rosen et al.³², our proteomics data revealed warming did not induce brown adipocyte cellular identity compared to RT (Fig. S2a–c). A total of 3,169 proteins were identified at all three temperature conditions (Fig. S2b). Among these proteins, we focused on analyzing those differentially expressed proteins between cold and TN (Fig. 3c). Global correlation analysis of the proteomics data revealed that BAT from mice housed at cold or TN were distinct (Fig. 3d). Notably, 1,964 proteins were downregulated, while 11 proteins related to whitening and inflammation^{33–35} were upregulated at TN compared to cold exposure (Fig. 3e and Fig. S2d). A pathway analysis revealed that these altered proteins were not only related to thermogenesis (Fig. S2e) but also to neurodegenerative diseases (NDs) such as PD and Huntington disease (Fig. 3f). Among these proteins, Park7, a familial gene associated with PD, was reported to play a role in metabolism^{22,24–26}. The immunoblotting revealed that the level of Park7 was decreased at TN (Fig. 3g). Secondly, we leveraging the computational interaction prediction capabilities of the STRING tool, which compiles information from various sources to form a meta-database, we identified 60 proteins that potentially interact with LAMP2A, each with a calculated confidence level of over 60% (Fig. S2f). Thirdly, The IP-MS revealed that 138 proteins interacted with LAMP2A (Fig. S2g). By combining the last two methods, we found that 4 proteins overlapped (Fig. 3h), and PARK7 was one of them. Fourthly, co-immunoprecipitation (Co-IP) and immunofluorescence further indicated that LAMP2A interacted and co-localized with PARK7 (Fig. 3i, j). Further experiment showed that LAMP2A could interact with PARK7 endogenously and the interaction was weaker under thermal stress (Fig. 3j, k). LAMP2A is a lysosomal transmembrane protein, and eleven amino acids at the C-terminal is located at cytoplasm. HSC70 was reported to interact with LAMP2A via this cytoplasmic region³⁶. Thus, we deleted this region, and found PARK7 could not interact with LAMP2A any more (Fig. 3l). In line with this, when overexpressed PARK7, LAMP2A and HSC70, LAMP2A could not bind to HSC70 (Fig. 3m), indicating PARK7 competes with HSC70 to interact with the cytoplasmic region of LAMP2A. Furthermore, according to structure prediction, 4 sites

of PARK7 were possibly binding to LAMP2A (Fig. 3n). The point mutations were generated and showed that E15, E18 and R48 were responsible for the interaction, but not H126 of PARK7 (Fig. 3o).

Furthermore, we studied whether PARK7 can regulate the expression of PGC1 α . In vitro studies revealed that transfection of Park7 increased the protein levels of PGC1 α and UCP1 in primary brown adipocytes and HEK 293 T cells, whereas knockdown of Park7 decreased their levels in HEK 293 T cells (Fig. 3p–r). However, double-knockdown of Park7 and Lamp2a increased the PGC1 α protein levels compared to Park7 knockdown (Fig. 3s). Mutants of KFERQ-like motifs in PGC1 α exhibited no alterations in cells with Park7 overexpression (Fig. 3t), demonstrating that PARK7 regulates the degradation of PGC1 α , possibly via CMA under thermal stress.

HSC70 competes with LAMP2A to bind to PARK7

On the other hand, we carried out IP-MS of PARK7 to further confirm the interaction. The IP-MS revealed that 95 proteins interacted with PARK7 (Fig. S3a). Surprisingly, except for LAMP2A, HSC70 was on the top 20 list (Fig. 4a). Therefore, we further addressed the relationship between HSC70 and PARK7. Co-IP assays revealed that HSC70 interacted with PARK7 (Fig. 4b). Immunofluorescence revealed that HSC70 co-localized with PARK7, and the co-localization was more significant when the cells were cultured at 39 °C (Fig. 4c). Fluorescence lifetime imaging microscopy (FLIM) assays revealed that τ -mean of PARK7 and HSC70 at 39 °C was much lower than those at 37 °C, indicating stronger interactions at TN (Fig. 4d). Co-IP in BAT lysate further confirmed that PARK7 could interact with HSC70 endogenously, and there were even more interactions at TN than RT (Fig. 4e). Next, we sought to further understand the structural basis for the interactions facilitating PARK7 and HSC70 recruitment and used the protein-protein interaction prediction algorithm AlphaFold2 (AF2) Multimer (<https://www.biorxiv.org/content/10.1101/2021.10.04.463034v2>) to predict the structure of the heterodimeric PARK7/HSC70 complex. The AF2 analysis predicted a high-confidence interaction between PARK7 and HSC70. PARK7/HSC70 were predicted to form high-ordered structures (Fig. S3b). PARK7 was predicted to bind to the HSC70 pockets and form an L-shaped interface with a rather large, buried surface area. The predicted L-shaped PARK7-HSC70 interface was highly charged with multiple conserved basic and acidic residues that had several electrostatic interactions (Fig. S3c). In the three putative electrostatic interactions located at the interface, the second contact, where the N terminal of PARK7 was highly involved, was located in the central region of the charged interface and may have contributed to the binding of PARK7 to HSC70 (Fig. 4f). Consequently, we generated point mutations in indicated sites and performed Co-IP assays. The assays revealed that R48, E15, and E18 (same sites for the interaction

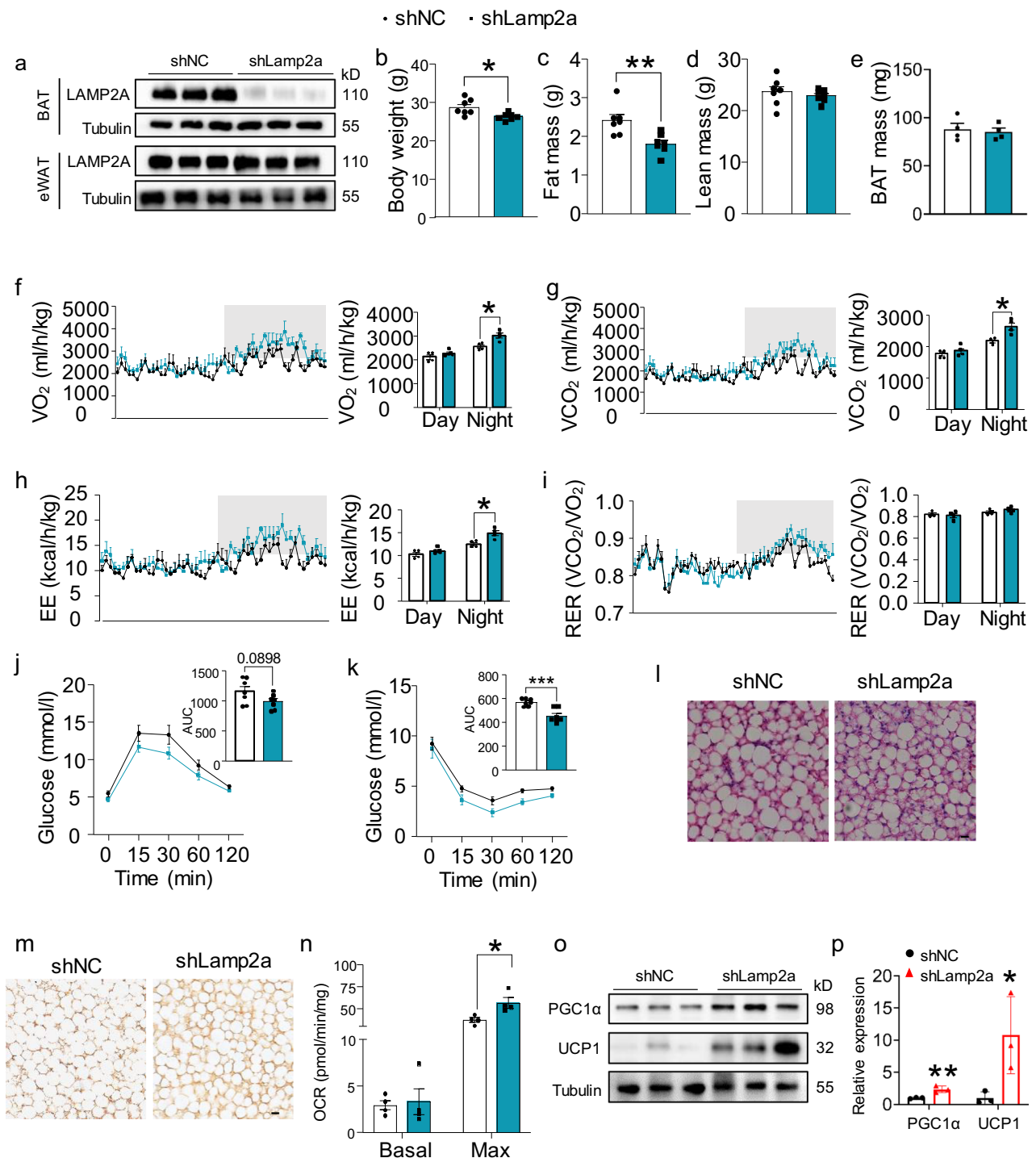
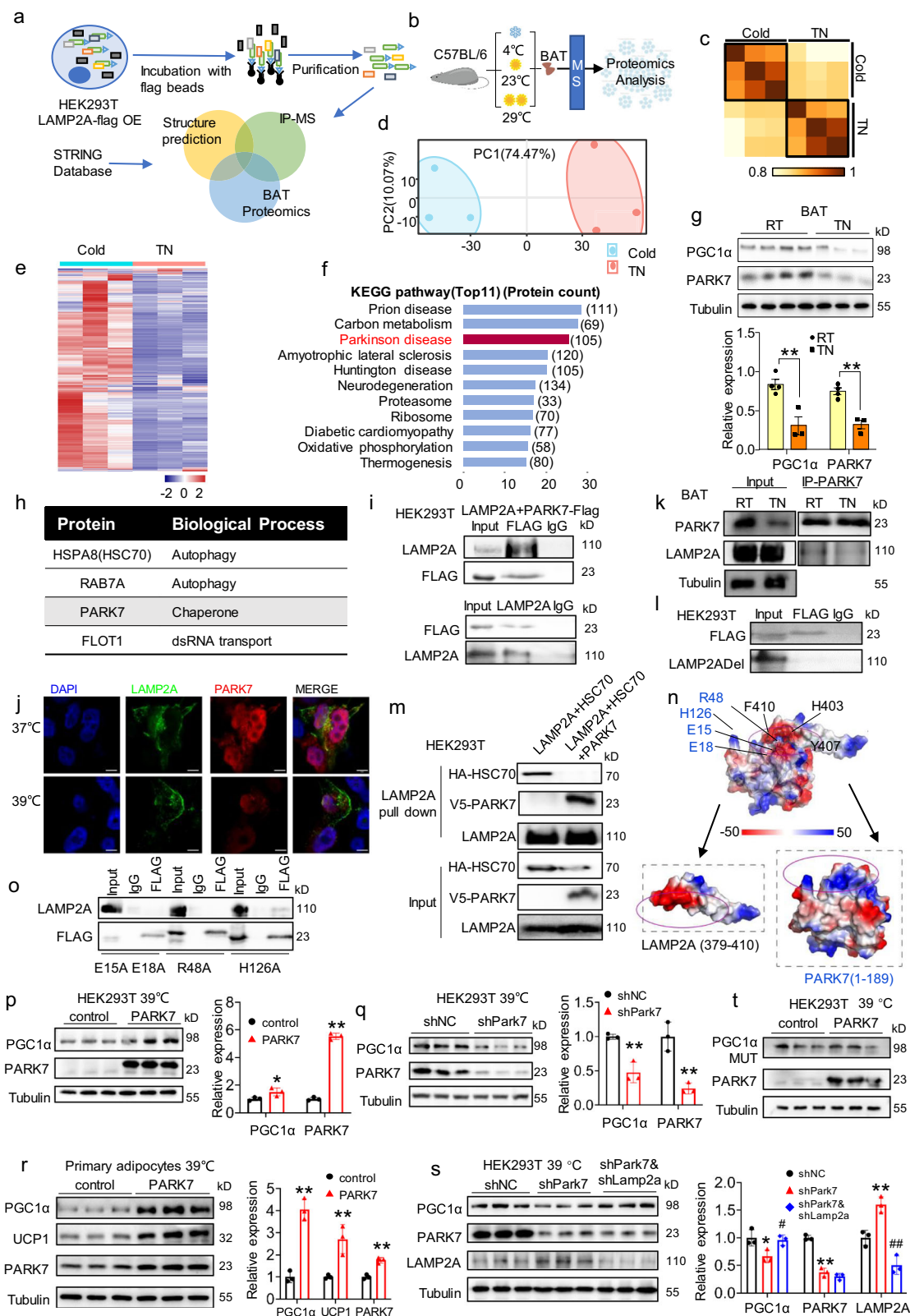


Fig. 2 | Mice with BAT-specific Lamp2a knockdown show identical energy metabolism at TN. **a** Immunoblotting for LAMP2A protein levels of BAT from male C57BL/6 mice 4 weeks after injection with AAV-shScramble or AAV-shLamp2a and totally housed at TN for 8 weeks. **b–j** Measurements of metabolic parameters of indicated mice housed at TN for 8 weeks, including body weight (**b**), $n = 7$ mice per group; fat mass (**c**), $n = 7$ mice per group; lean mass (**d**), $n = 7$ mice per group; BAT mass (**e**), $n = 4$ mice per group; oxygen consumption and quantitation of oxygen consumption (**f**), $n = 4$ mice per group; carbon dioxide production and quantitation of carbon dioxide production (**g**), $n = 4$ mice per group; EE and quantitation of EE (**h**), $n = 4$ mice per group; RER and quantitation of RER (**i**), $n = 4$ mice per group; GTT

and AUC of GTT (**j**), $n = 7$ mice per group; ITT and AUC of ITT (**k**), $n = 7$ mice per group. **l, m** Histochemistry analysis, including representative hematoxylin-eosin staining of BAT (**l**), representative immunohistochemical UCP1 staining of BAT (**m**). Scale bar, 20 μm. **n** OCR analysis of BAT ($n = 4$ mice per group). **o** Immunoblotting for PGC1α and UCP1 protein levels of BAT lysate (representative of $n = 3$ independent experiments). **p** Quantification of **o**. Statistical significance was assessed by unpaired Student's *t*-test. All results were expressed as means ± SEM, * $p < 0.05$, ** $p < 0.01$, *** $p < 0.005$. Student's two-tailed unpaired *T*-test for 2-group comparisons. Source data are provided as a Source Data file.



between LAMP2A and PARK7) of PARK7 contributed to the interaction with HSC70, while M17 did not play a role (Fig. 4g). Furthermore, overexpression of PARK7R48A or E15AE18A failed to increase PGC1α protein levels (Fig. 4h). Similarly, the co-localization of PARK7 and HSC70 was reduced when these PARK7 mutants were transfected (Fig. 4i). To further confirm whether HSC70 competes with LAMP2A to interact with PARK7, we conducted dose-dependent experiments. As the levels of PARK7 increased, the binding protein levels of LAMP2A

decreased (Fig. 4j). These findings indicated that HSC70 interacts with PARK7, and sites R48, E15, and E18 are crucial for this effect.

Mice with BAT-specific Park7 knockout show lower energy metabolism at TN

Since PARK7 can both interact with LAMP2A and HSC70, and regulate the activity of CMA at TN, we produced BAT specific Park7 knockout mice by crossing UCP1-cre with Park7 Flox mice (hereafter as

Fig. 3 | PARK7 interacts with LAMP2A and regulates PGC1 α degradation. **a** The schematic of Co-IP mass spectrum, protein interaction prediction and brown adipose tissue (BAT) proteomics. **b** The schematic of proteomics. **c** Principal-component analysis of the BAT proteomics dataset. **d** Similarity matrix showing Spearman correlations for proteomics dataset profiles. Spearman correlation coefficient r is represented in color as indicated. **e** Heatmap of BAT proteomics data detected in cold and warm conditions. **f** KEGG pathway analysis of significantly different BAT proteins in cold condition *vs* warm condition. **g** Immunoblotting for PARK7, PGC1 α protein levels in BAT from mice housed at room temperature (RT, 23 °C) or thermoneutrality (TN, 29 °C) and quantification (bottom) (representative of $n = 3$ independent experiments). **h** Overlapping the data from Co-IP mass spectrum and protein interaction prediction. **i** Co-IP analysis of FLAG and LAMP2A in HEK293T cells co-expressing Flag-Park7 and Lamp2a. **j** Colocalization analysis of PARK7 and LAMP2A at 37 °C and 39 °C in HEK293T cells. Scale bar, 5 μ m. **k** Endogenous Co-IP analysis of PARK7 and LAMP2A in BAT from mice housed at RT and TN. **l** Co-IP analysis of FLAG and LAMP2A in HEK293T cells co-expressing Flag-Park7 and Lamp2aDel. **m** Co-IP analysis of the competitive combination of PARK7

and LAMP2A with HSC70 in HEK293T cells co-expressing Lamp2a and HA-Flag-Hsc70 with or without V5- Park7. **n** 3D structure prediction of mouse protein interaction between LAMP2A and PARK7. **o** Co-IP assays of PARK7 mutants R48A, E15AE18A, H126A and LAMP2A in HEK293T cells co-expressing Flag-Park7 mutants and Lamp2a. **p, q** Immunoblotting for PARK7 and PGC1 α protein levels in HEK293T cells with overexpression or knockdown of Park7 in 39 °C for 24 h (representative of $n = 3$ independent experiments). **r** Immunoblotting for PARK7, PGC1 α and UCP1 protein levels in primary brown adipocytes with overexpression of Park7 (representative of $n = 3$ independent experiments). **s** Immunoblotting for PGC1 α , PARK7 and LAMP2A protein levels in HEK293T cells knockdown of Park7 and Lamp2a in 39 °C for 24 h (representative of $n = 3$ independent experiments). **t** Immunoblotting for PGC1 α and PARK7 protein levels in HEK293T cells co-expressing PARK7 and PGC1 α -MUT in 39 °C for 24 h (representative of $n = 3$ independent experiments). Statistical significance was assessed by unpaired Student's *t*-test. All results were expressed as means \pm SEM and $^{**}p < 0.01$. Student's two-tailed unpaired *T*-test for 2-group comparisons. Source data are provided as a Source Data file. Figures **a, b** were created using PowerPoint.

Park7^{ΔUcp1}) to investigate its roles in BAT (Figs. 5a, b, and S4a, b). Initially, we characterized the metabolic physiology of Park7^{ΔUcp1} mice under standard housing conditions. In this setting, Park7^{ΔUcp1} and Flox mice had identical body weight, body mass composition, and energy expenditure (Fig. S4c, m). However, when we housed Park7^{ΔUcp1} mice at TN, both male and female Park7^{ΔUcp1} mice gained more weight compared to the Flox control mice on a normal chow diet (Fig. 5c and Fig. S4n–r). The increased weight gain in the Park7^{ΔUcp1} mice was primarily due to higher fat mass, while lean mass remained comparable between the two groups (Fig. 5d, e). We then assessed the metabolic phenotypes at TN. We applied metabolic cage measurements to assess whole-body energy expenditure. The Park7^{ΔUcp1} mice had lower rates of oxygen consumption (VO₂), CO₂ production (VCO₂), and energy expenditure (EE) than the Flox mice (Fig. 5f–h). However, their energy intake, respiratory exchange ratio (RER), and locomotor activities were comparable (Fig. S5s–u). Furthermore, glucose and insulin tolerance tests revealed that the Park7^{ΔUcp1} mice had poorer glucose and insulin tolerance (Fig. 5i, j). These findings indicated that the loss of Park7 in BAT impairs energy metabolism upon thermal acclimation.

Next, we investigated the role of Park7 in the modulation of whole-body energy expenditure during diet-induced obesity (DIO). We found that *Park7* expression in human adipose tissue was negatively correlated with body mass index (BMI) and homeostasis model assessment of insulin resistance (HOMA-IR) (Fig. 5k, l)³⁷. The protein levels of Park7 were down-regulated in BAT from DIO or diabetic mice (Fig. 5m, n). We then housed the Park7^{ΔUcp1} mice at RT and subjected them to a high-fat diet (HFD) for 12 weeks. Both Flox and Park7^{ΔUcp1} mice gained considerable and indistinguishable weight and fat mass on the HFD (Fig. S5a–f). Nevertheless, the EM revealed that the majority of mitochondria were enlarged with loose cristae in Park7 knockout adipocytes (Fig. S5g).

Thermoneutral housing in combination with HFD can be used to thermally humanize mice³⁸, and BAT from mice housed under such conditions remarkably resembles human BAT^{3,38}. Park7^{ΔUcp1} mice were therefore housed under physiologically humanized conditions to characterize their metabolic phenotypes. Notably, the Park7^{ΔUcp1} mice gained more weight and increased fat mass compared to the Flox mice at TN (Fig. 5o–w). The weight gain was not because of increased food intake but decreased energy expenditure (Fig. 5r–u). The Park7^{ΔUcp1} mice exhibited impaired glucose tolerance but not insulin tolerance compared to the Flox mice (Figs. 5v and S5h). Although the brown adipocytes seemed to be whitening under physiologically humanized conditions, the Park7^{ΔUcp1} mice had even larger adipocytes with bigger lipid droplets (Fig. 5w).

Park7 ablation exacerbates BAT whitening at TN

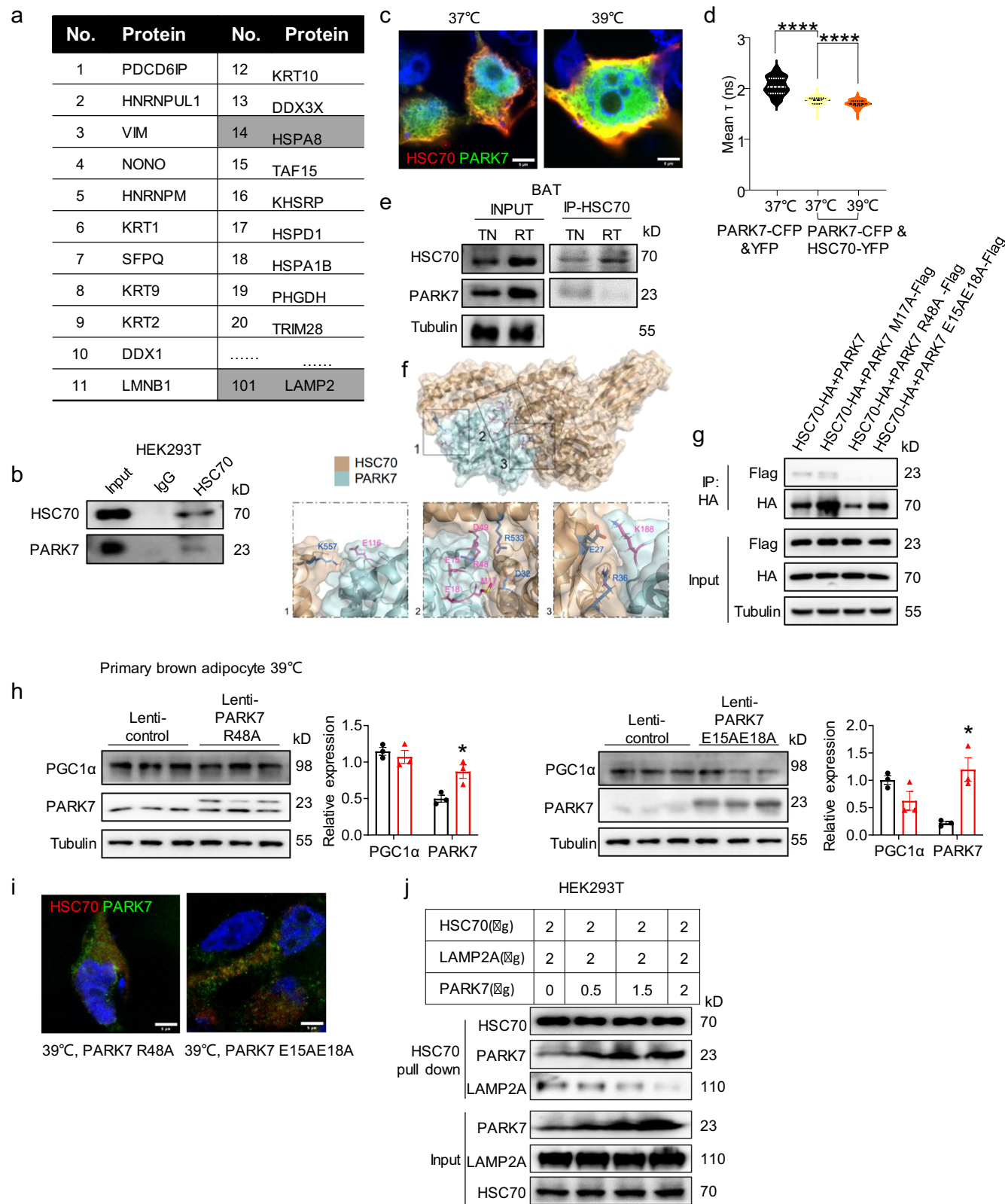
To further explore the role of Park7 in BAT physiology, various imaging studies were conducted, including hematoxylin and eosin (H&E)

staining, immunohistochemistry (IHC) for UCP1 and crown-like structure (CLS), and electron microscopy (EM). The Park7^{ΔUcp1} mice exhibited larger adipocyte areas and weaker UCP1 staining compared to the control mice (Fig. 6a, b) at TN, indicating that Park7 ablation aggravated BAT whitening. Furthermore, warm acclimation induced the formation of CLS in BAT¹⁵. We subsequently stained BAT with F4/80 and observed more CLSs in the BAT lacking Park7 compared to the control group (Fig. 6c). Moreover, brown adipocytes filled with numerous mitochondria packed with laminar cristae at TN, and mitochondria from Park7^{ΔUcp1} mice exhibited signs of degeneration characterized by the absence of cristae and broken membrane (Fig. 6d). The protein levels of some mitochondrial genes (*Atp5a*, *Uqcrc2*, *Sdhb*, and *Ndufb8*) were significantly decreased in Park7 knockout BAT at TN (Fig. 6e). The oxygen consumption rate was also suppressed in Park7 knockout BAT (Fig. 6f), suggesting a lack of Park7 impairs mitochondrial morphology and function at TN.

To further analyze the molecular signaling changes in BAT, we performed RNA-seq assays on BAT. The analysis revealed 3922 differentially expressed genes (DEGs) between the genetic models at TN (Fig. 6g and Fig. S6a). The Gene Ontology (GO) pathway analysis suggested that lipid catabolic process was increased and angiogenesis was decreased in the Park7^{ΔUcp1} mice at TN (Figs. 6h and S6b). Among the DEGs, white adipose tissue genes (*Adipoq*, *Cebpa*, *Pank3*, and *Pparγ*) and inflammatory genes (*Ccl5*, *Il10rb*, and *Il6ra*) were increased in the Park7^{ΔUcp1} mice at TN (Fig. 6i). These findings were further confirmed by quantitative polymerase chain reaction (QPCR) (Fig. 6j). Surprisingly, thermogenic and fatty acid oxidation (FAO) genes were also increased in the Park7^{ΔUcp1} mice compared to Flox mice at TN (Fig. 6j). Nonetheless, the protein levels of thermogenic genes (PGC1 α and UCP1) were decreased, without alterations in FAO proteins in the Park7-knockout BAT (Fig. 6k).

4-Phenylbutyric acid (4-PBA) and comp23 increase and decrease BAT activity, respectively

4-PBA was reported to dramatically increase Park7 expression³⁹. By treating the HEK293T cells with 4-PBA, we found that the protein levels of PARK7 and PGC1 α were increased (Fig. S7a). Therefore, we injected 4-PBA directly into the BAT, while monitoring energy expenditure and metabolic parameters using indirect calorimetry (Fig. S7b–e). Notably, the Flox mice exhibited enhanced energy expenditure responses to 4-PBA, but the effects were diminished in the Park7^{ΔUcp1} mice (Fig. S7B–D). Moreover, the BAT from the Park7^{ΔUcp1} mice had a blunted respiratory response to 4-PBA compared to that from controls (Fig. S7f, g). The protein levels of PGC1 α and UCP1 were increased in wild-type BAT treated with 4-PBA but were not altered in Park7 knockout samples (Fig. S7h), suggesting that 4-PBA enhances BAT activity depending on the presence of Park7.



Comp23 was reported to bind to Park7 to inhibit its activity⁴⁰. We previously demonstrated that comp23 mimics the effects of Park7 ablation in skeletal muscles in vivo⁴¹. To assess the role of comp23 in BAT, we treated brown adipocytes in vitro and in vivo with comp23. PGC1 α and UCP1 expression were downregulated in the comp23-treated cells and BAT (Fig. S7i, j). However, the effects were diminished in Park7 ablated BAT (Fig. S7j). Mitochondrial oxygen consumption

was decreased upon comp23 treatment in the Flox mice but not in the Park7^{ΔUcp1} mice (Fig. S7k, l). To investigate whether comp23 binds to Park7 and subsequently inhibits the interaction between Park7 and HSC70, we performed a Co-IP assay. As expected, the interaction between Park7 and HSC70 was weaker, whereas the interaction between HSC70 and LAMP2A was stronger when treated with comp23 (Fig. S7m).

Fig. 4 | HSC70 competes with LAMP2A to bind to PARK7. **a** Table of top 20 proteins and LAMP2A from Co-IP mass spectrum. **b** Co-IP analysis of PARK7 and HSC70 in HEK293T cells co-expressing V5-Park7 and HA-Flag-Hsc70. **c** Colocalization analysis of PARK7 and HSC70 at 37 °C and 39 °C in HEK293T cells co-expressing HA-Flag-Hsc70 and Flag-Park7. **d** Quantitative analysis of fluorescence lifetime imaging microscopy (FLIM) of CFP fluorescence in HEK293T cells co-expressing CFP-Park7 and YFP-Hsc70 ($n = 75$). **e** Endogenous co-immunoprecipitation analysis of PARK7 and HSC70 in BAT from mice housed at RT and TN. **f** Multiple electrostatic interaction groups are involved in the surface of PARK7/HSC70 complex to maintain the L-shape interface according to the electrostatic properties of the residues. Residues of HSC70 involved were indicated and colored in blue as residues of PARK7 involved were colored in red, respectively. **g** Co-IP assays of PARK7 mutants M17A,

R48A and E15AE18A and HSC70 in HEK293T cells co-expressing Flag-Park7 WT/ mutants and HA-Flag-Hsc70. **h** Immunoblotting for PGC1 α and PARK7 protein levels in primary brown adipocytes when overexpressing Park7 mutants in 39 °C for 24 h (representative of $n = 3$ independent experiments). **i** Colocalization analysis of PARK7 mutants R48A and E15AE18A and HSC70 at 39 °C in HEK293T cells. Scale bar, 5 μ m. **j** Co-IP analysis of the competitive interaction among PARK7, LAMP2A and HSC70 in HEK293T cells. Cell lysates from HEK293T cells transfected with 2 μ g HSC70 and 2 μ g LAMP2A with and without different amount PARK7 were used for IP and IB assays. Statistical significance was assessed by unpaired Student's t -test. All results were expressed as means \pm SEM and **** $p < 0.001$. Student's two-tailed unpaired T -test for 2-group comparisons. Source data are provided as a Source Data file.

CMA is required for Park7 ablation-induced BAT whitening

To investigate whether the role of Park7 in BAT depends on the activity of CMA, we injected AAV-shLamp2a into the BAT of the Park7^{ΔUcp1} mice (Fig. 7a) and housed them at TN. Four weeks after the injection, the Park7^{ΔUcp1} mice with Lamp2a knockdown gained similar weight as the Flox control mice, lighter than the Park7^{ΔUcp1} mice (Fig. 7b). Similarly, the fat mass was lower in the Park7^{ΔUcp1} mice with shLamp2a compared to the mice injected with AAV-shScramble; however, there were no significant differences in lean mass (Fig. 7c, d). Additionally, we assessed whole-body energy expenditure and found that Lamp2a knockdown rescued the VO₂, VCO₂, and energy expenditure (Fig. 7e–g). Consistent with this finding, glucose and insulin tolerances were restored to normal when CMA activity was decreased (Fig. 7h, i).

Further investigation on adipose biology revealed that the knockdown of Lamp2a in the Park7^{ΔUcp1} mice restored the adipocyte size and CLS (Fig. 7j, k). UCP1 staining revealed increased UCP1 positive cells in the Park7^{ΔUcp1}+shLamp2a group compared to the Park7^{ΔUcp1}+shScramble group (Fig. 7l). In addition, the mitochondrial oxygen consumption rate was restored when AAV-shLamp2a was injected into the BAT of the Park7^{ΔUcp1} mice (Fig. 7m). The protein levels of PGC1 α , UCP1, and OXPHOS exhibited the same changes (Fig. 7n), confirming that CMA activity is required for the Park7 ablation-induced BAT dysfunction.

These findings suggest that CMA can regulate the degradation of PGC1 α at TN. PARK7 can sense the temperature changes, and bind to LAMP2A or HSC70 depending on the temperature, subsequently affect CMA. Park7 ablation aggravates BAT whitening at TN by enhancing the activity of CMA, eventually regulates energy metabolism.

Discussion

CMA activity is considerably upregulated under stress conditions such as prolonged nutrient deprivation (serum removal in cultured cells or starvation in rodents)⁴² and mild oxidative stress^{43,44}. In this study, we found that CMA activity was induced by thermal stress in BAT. The enhanced CMA can selectively degrade PGC1 α . Impaired CMA in BAT improved the metabolic phenotypes at TN. PARK7 is evidenced to sense the temperature changes and regulate the CMA activity through binding to LAMP2A or HSC70. Mice with Park7 ablation exhibited increased body weight and fat mass, decreased energy expenditure, and impaired insulin sensitivity at TN. Park7 ablation destroyed the mitochondrial morphology and function and suppressed thermogenic proteins but increased the expression of white adipogenic and inflammatory genes. Knockdown of Lamp2a in BAT reversed the effects induced by Park7 ablation.

PGC1 α is a master regulator of cellular energy metabolism. PGC1 α co-activates multiple transcription factors involved in mitochondrial biogenesis, fatty acid oxidation, and thermogenesis, especially in BAT and muscle where it governs many aspects of fuel metabolism and ATP production¹¹. Given the potency of this co-activator, its expression and activity must be controlled in accordance with energy demands and substrate availability. Our data herein demonstrated that PGC1 α is degraded through CMA under thermal stress. Using KFERQ-like motifs

mutants of PGC1 α can stabilize the protein. In vivo studies exhibited that the protein levels of PGC1 α -targeted genes showed similar changes to PGC1 α , including UCP1, ATP5A, UQCRC2, MTCO1, SDHB and NDUFB8.

The selectivity of CMA seems beneficial under conditions requiring discrimination between different types of proteins for degradation. For example, the degradation of proteins via CMA will provide cells with free amino acids required to sustain protein synthesis under prolonged starvation^{42,45}. Likewise, under thermal stress, thermogenic activity is not required for the mice to maintain body temperature⁴⁶, so thermogenic proteins may be degraded via CMA for other survival processes. In this study, we found that thermogenic proteins-PGC1 α was degraded by CMA, whose activity was enhanced by Park7 ablation under thermal exposure. In addition, thermal stress and Park7 ablation can both cause oxidative stress^{47,48}, which may subsequently further activate CMA.

CMA is a multistep process that results in selective degradation of intracellular soluble proteins⁴⁹. HSC70 recognizes substrates containing KFERQ-like motifs and presents the proteins to the surface of a subset of lysosomes, where they bind to LAMP2A and undergo autophagic degradation. While the signaling mechanisms leading to CMA activation/inactivation are not well understood, most of the regulation of this pathway occurs in the lysosomal compartment^{50–53}. PARK7 competes with HSC70 for the binding site of LAMP2A, thereby blocking the binding of LAMP2A to HSC70 and eventually affecting the activity of CMA.

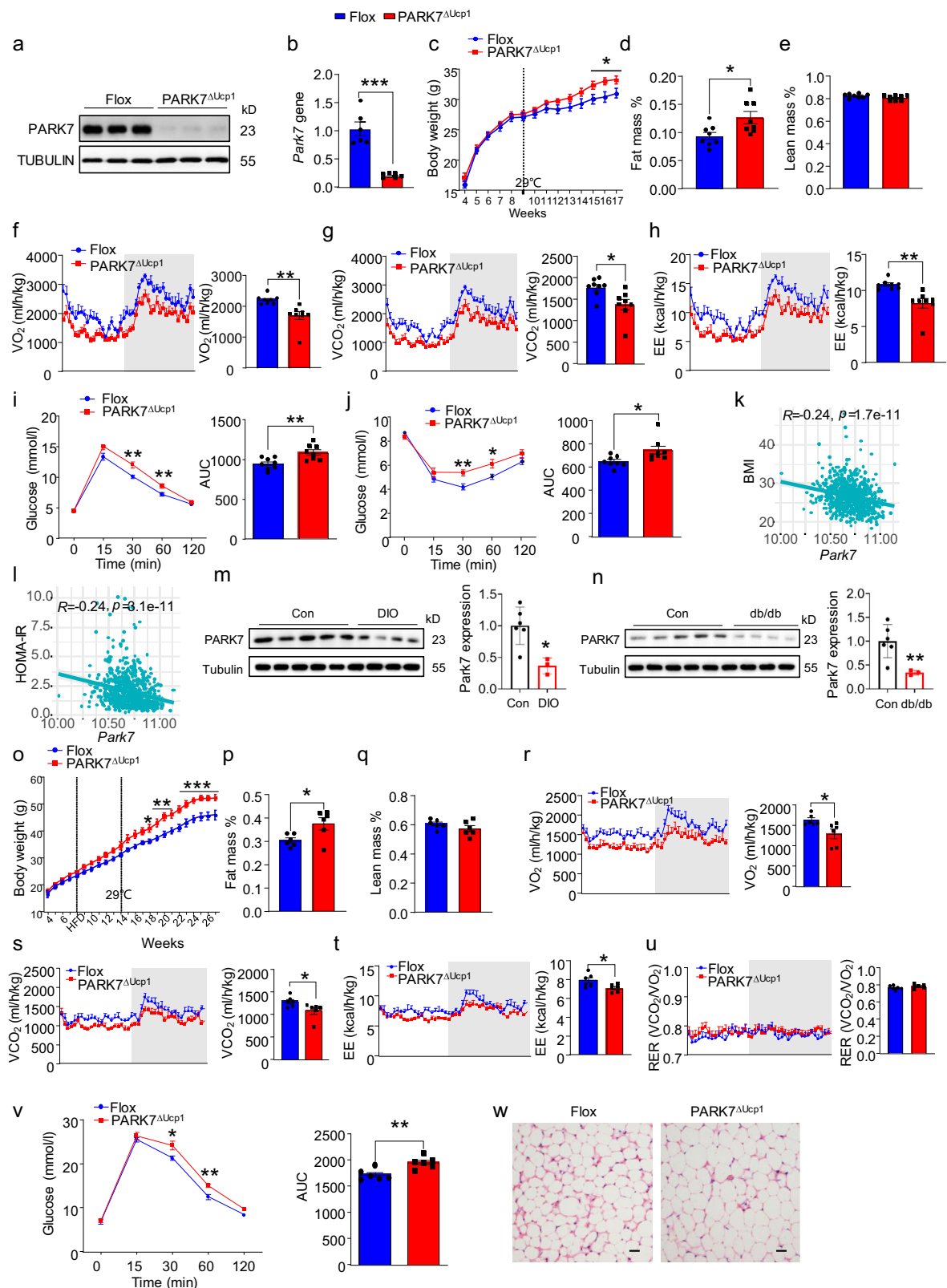
The Lamp2a-knockdown mice exhibited improved metabolic phenotypes compared to the control mice when housed at TN. On the other hand, the Park7^{ΔUcp1} mice gained more weight than the control mice at TN. This highlighted the similar phenotypes observed in UCP1 knockout mice⁵⁴. Consistent with this finding, the protein levels of UCP1 were significantly decreased in the BATs with Park7 ablation. Additionally, BAT whitening was induced under thermal acclimation, with increased unilocular adipocytes, CLS, and degenerated mitochondria⁵⁵. Genetic or pharmacological inhibition of PARK7 aggravated the whitening effects. The enhanced CMA activity was responsible for these phenotypes, but other mechanisms could be involved as well, including mitophagy, since PARK7 acts in parallel to PINK1/parkin-mediated mitophagy^{48,56}. Resultantly, further studies need to be performed in the future.

Our study sheds light on the key role of CMA in the maintenance of BAT energy homeostasis at TN. We provide direct evidence that PARK7 regulates the interaction between LAMP2A and HSC70, affecting the activity of CMA and eventually regulating the stability of thermogenic proteins in BAT. Thus, we establish a pathway that could be targeted to prevent the loss of BAT thermogenic capacity in adult humans.

Methods

Mice

The Park7^{flox/flox} strain was generated in our previous studies⁴¹. UCP1-Cre strain was obtained from Jax lab. To generate UCP1-cre^{+/+}; Park7^{flox/flox} mice (Park7^{ΔUcp1}) and UCP1-cre^{+/+}; Park7^{flox/flox} (Flox), UCP1-cre mice were breed with Park7^{flox/flox} mice. Unless



otherwise stated, male mice were utilized in the study, and they were housed in a 12/12 h light-dark cycle with free access to food and water at an ambient temperature of $22 \pm 1^\circ\text{C}$. For diet-induced obesity studies, the mice were fed a high-fat diet (Research Diets, D12492) for 12 weeks. In the thermoneutral experiments, 8-week-old mice were housed in a 29°C rodent chamber for 8 weeks. Body weight was recorded once a week. For the in situ AAV injection into

the BAT, the mice were anesthetized with isoflurane and positioned prone. The interscapular BAT was exposed by shaving the shoulder region and cutting the skin. A total of $50 \mu\text{L}$ AAV-GFP-shLamp2a or AAV-GFP scramble were evenly injected into BAT. Two weeks following the injection, the mice were treated as mentioned above. Western blot analysis was conducted to verify virus infection and expression efficiency in mice. Animal

Fig. 5 | Mice with BAT-specific *Park7* knockout show lower energy metabolism at TN. **a, b** Protein and mRNA levels of *Park7* in the BAT from male *Park7^{ΔUcp1}* and Flox mice. **c–j** Measurements of metabolic parameters of male *Park7^{ΔUcp1}* and Flox mice housed at TN for 8 weeks, including body weight (**c**), fat mass to body weight ratio (**d**), lean mass to body weight ratio (**e**), oxygen consumption (VO_2) and quantitation of VO_2 (**f**), carbon dioxide production (VCO_2) and quantitation of VCO_2 (**g**), energy expenditure (EE) and quantitation of EE (**h**), glucose tolerance test (GTT) and area under curve (AUC) of GTT (**i**), insulin tolerance test (ITT) and AUC of ITT (**j**) ($n = 8$). **k, l** Association between BMI (**k**) or HOMA-IR (**l**) and *Park7* expression level in human from the METSIM study. **m** Immunoblotting and quantitation for PARK7 protein in BAT from diet-induced obesity (DIO) mice. $n = 5$ for control group

and $n = 4$ for DIO group. **n** Immunoblotting and quantitation for PARK7 protein in BAT from db/db mice. $n = 5$ for control group and $n = 4$ for db/db group. **o–w** Analysis of metabolic phenotypes of male *Park7^{ΔUcp1}* and Flox mice on HFD housed at TN for 8 weeks, including body weight (**o**), fat mass to body weight ratio (**p**), lean mass to body weight ratio (**q**), VO_2 and quantitation of VO_2 (**r**), VCO_2 and quantitation of VCO_2 (**s**), EE and quantitation of EE (**t**), RER and quantitation of RER (**u**), GTT and AUC of GTT (**v**) ($n = 6$). **w** Representative hematoxylin-eosin staining of BAT from male *Park7^{ΔUcp1}* and Flox mice on HFD housed at TN for 8 weeks. Scale bar, 20 μm . Statistical significance was assessed by unpaired Student's *t*-test. All results were expressed as means \pm SEM and $^*p < 0.05$, $^{**}p < 0.01$. Student's two-tailed unpaired *T*-test for 2-group comparisons. Source data are provided as a Source Data file.

experiments were conducted in accordance with the institutional Animal Care and Use Committee of Shanghai University of Sport, which approval all animal study protocols.

Glucose tolerance test and insulin tolerance tests

For the glucose tolerance test (GTT), animals were fasted overnight with water available, and for the insulin tolerance test (ITT), they were fasted for 6 h with water available. Fasting blood glucose levels were measured before intraperitoneal (IP) injection of glucose (1.5 g/kg weight) or insulin (0.75 U/kg weight). Blood glucose levels were measured at different time points (15, 30, 60, and 120 min).

Body composition and energy metabolism measurement

Body weight was measured weekly. A body composition analyzer (Brucker) was used to determine body composition (fat mass and lean mass). For metabolic studies, mice were individually housed in metabolic cages with free access to food and water. Oxygen consumption and CO_2 production rates were monitored for 48 h using CLAMS (Columbus Instruments). Food intake monitoring was performed simultaneously with metabolic measurements.

BAT mitochondrial respiration studies

BAT was excised, cut into 2–2.5 mg weight and put into ice cold MIROS (0.5 mM EGTA, 3 mM MgCl_2 , 60 mM lactobionic acid, 20 mM taurine, 10 mM KH_2PO_4 , 20 mM HEPES, and 110 mM D-sucrose) and homogenized. After homogenization, the solution of BAT were added into the O2K chambers; 5 mM pyruvate, 2 mM malate and 10 mM glutamate (PMG) were added for; 1 M succinate (SUC) was added for complex II; 0.2 M N,N,N',N'-tetramethyl-p-phenylenediamine dihydrochloride (FCCP) for maximal respiration flux; 0.5 μM rotenone (ROT) was added for inhibiting complex I; 2.5 μM antimycin A (AMA) was added for inhibiting complex III.

Cold tolerance test

For cold exposure experiments, individual mice were placed in single cages in a cold room (4 °C) with free access to water. Control mice were kept at room temperature (22 °C). The core body temperature was monitored using a rectal probe at each time point. For chronic cold exposure, mice were first subjected to 3 days of intermittent cold exposure (12 h at 4 °C in the light cycle and 12 h at room temperature) followed by 7 days of continued cold exposure at 4 °C.

Cell lines

HEK 293 T cell line was obtained from ATCC and cultured in Dulbecco's modified eagle medium (DMEM) supplemented with 10% fetal bovine serum, 100 $\mu\text{g}/\text{mL}$ of streptomycin, and 100 U/mL of penicillin at 37 °C in 5% CO_2 .

Differentiation of primary preadipocytes

For isolation of BAT stromal vascular fractions (SVFs), BAT from 2-week-old mice was digested for 60 min at 37 °C by collagenase I (Sigma-Aldrich, C5138) in 1X PBS with BSA (10 mg/ml). The digested

cell suspension was centrifuged and the pelleted cells were resuspended, and filtered through a 75- μm cell strainer. Then the SVF cells were plated on 6-well plates in DMEM supplemented with 10% FBS and 1% P/S at 37 °C in a humidified 5% CO_2 incubator. When the cells were confluent, the cell medium was replaced by differentiation Medium (0.1 $\mu\text{g}/\text{mL}$ insulin and 1 nM T3), and 48 h later, cells were changed to induction medium (0.1 $\mu\text{g}/\text{mL}$ insulin, 1 nM T3, 125 mM indomethacin, 5 μM dexamethosone, 0.5 mM 3-isobutyl-1-methylxanthine) for another 2 days.

Plasmid DNA and lentivirus

We constructed the mutant plasmids by Mut Express II Fast Mutagenesis Kit V2 (Vazyme). The primers for mutation are as followed: park7 E15A E18A F- GCAGcggagatggcgACAGTGATTCTGTGGATGT CATGCG; park7 E15A E18A R- ACTGTcgccatctccgcTGCTCCTTTGGC-CAGGATG; park7 R48A F- GTGTAGCgctGATGTAATGATTTGTCCAGATACCAGT; park7 R48A R- TTACATCagcGCTACACTGCACGGGGTCC TTC; park7 H126A F- TCACAACAgccCCACTGGCTAAGGACAAAATGA; park7 H126A R- CAGTGGggcTGTTGTGACCTTGATCCAAAAC.

PGC1 α 408MUT F: TCTAGAgcagcaGACTTCAAAGATGCCTCC TGTGA

PGC1 α 408MUT R: GAAGTctgtgcTCTAGAGTCTTGAGCTCCT GTGA

PGC1 α 492MUT F: ATGAAGcagccTCCAAACTACCTGTGTTTATAA ATTCAG

PGC1 α 492MUT R: GTTTGGAggctgcTTCATTACTGAAGTCGCCA TCCC

PGC1 α 754MUT F: ACGGAAGgcagctTTCAGTCTAACTATGCA GACCTAGATACC

PGC1 α 754MUT R: TTGAAGctgcCTTCGTCACAAAAGTACA GCT

PGC1 α 792MUT F: TgcggcaAGCTTTCTAGAACAAAACTCATC TCA

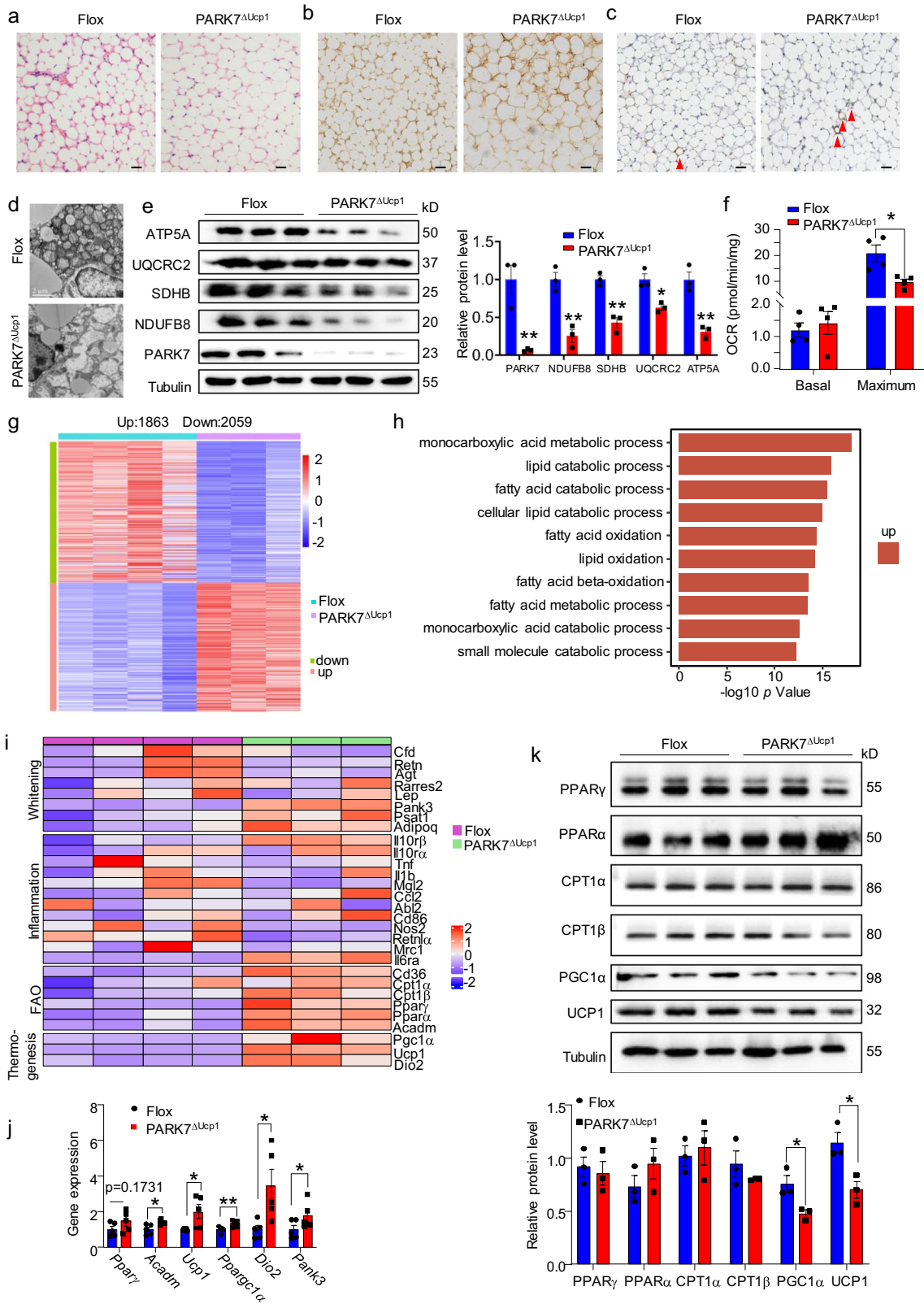
PGC1 α 792MUT R: TCTAGAAAGCTtgccgcAGCTTCCTTCAGTAA ACTATCAAAATCC

We deleted LAMP2A406–415aa from PCDH-LAMP2A(mouse), the primers are as followed: Hind3 mL2A F- GAACAAGCTTGCCACCATGTG CCTCT; truncate Xho1 mL2A R- GAACCTCGAGACCAATAAAAA-TAAGCCAGCAAC. PCDH-LAMP2A(mouse), PCDH-HSC70-HA-FLAG (mouse) were gifts from Dr Yi Xu (Fudan University), PCDH-PARK7-Flag(mouse) was constructed by wildtype C57 BAT cDNA, the primers are as followed: Park7M F: XbaI- GAACCTCTAGAACCATGGCTT; Park7M R: EcoRI- GAACGAATTCGCTCTTTGAGAACAAG.

Plasmid DNA was transfected into HEK 293 T cells using PEI reagent (PolySciences, 23966-100) according to the manufacturer's protocol. Cell lysate was extracted after 2-days transformation. Lentivirus was added to SGBS cell and primary preadipocytes after differentiation, and add medium after 12-h infection. Cell lysate was extracted after 2-days infection.

Cell treatment

For PGC1 α degradation detection, cells were treated with 50 μM cycloheximide (CHX) for 3 h. For proteasome inhibition, cells were



treated with MG132, 25 μ M 4 h for HEK 293 T cells and 10 μ M 24 h for primary preadipocytes. For autophagy inhibition, cells were treated with chloroquine (CQ), 200 μ M 7 h for HEK 293 T cells and 50 μ M 24 h for primary preadipocytes. For PARK7 activation, cells were treated with 0.5 mM 4-phenylbutyric acid (4-PBA) for 24 h. For PARK7 inhibition, cells were treated with 2 μ M comp23 for 24 h. For CMA activation, cells were treated with 20 μ M Qx77 for 24 h.

KFERQ-like motif prediction

By KFERQ finder V8.0 (<https://rshine.einsteinmed.edu/>)⁵⁷, protein sequences are from Uniprot (<https://www.uniprot.org/>).

Immunoblot analysis and immunoprecipitation and antagonist

To prepare lysates for immunoblot analysis, cells or tissues were treated with RIPA buffer (Beyotime, P0013B) containing complete

Fig. 6 | Park7 ablation exaggerates BAT whitening at thermoneutrality.

a–c Histochemistry analysis of BAT of male Park7^{ΔUcp1} and Flox mice housed at TN for 8 weeks, including hematoxylin-eosin staining (**a**), immunohistochemical staining of UCP1 (**b**) and F4/80 (**c**). Arrow indicated crown-like structure. Scale bars, 20 μm. **d** Representative EM images of BAT from male Park7^{ΔUcp1} and Flox mice housed at TN for 8 weeks. Scale bars, 2 μm. **e** Immunoblotting for mitochondrial proteins in BAT from male Park7^{ΔUcp1} and Flox mice housed at TN for 8 weeks ($n = 3$ mice per group). **f** Oxygen consumption rate (OCR) analysis of BAT from male Park7^{ΔUcp1} and Flox mice housed at TN for 8 weeks ($n = 4$). **g–i** RNA-seq analysis of BAT from male Park7^{ΔUcp1} and Flox mice housed at TN for 8 weeks, including

heatmap of all changed genes (**g**), GO pathway analysis of up-regulated pathways (**h**), heatmap of whitening, thermogenesis, inflammation, fatty acid oxidation genes (**i**). **j** QPCR analysis for mRNA levels of *Pparγ*, *Acadm*, *Ucp1*, *Ppargc1a*, *Dio2*, *Pank3* of BAT from male Park7^{ΔUcp1} and Flox mice housed at TN for 8 weeks ($n = 5$). **k** Immunoblotting for protein levels of PPAR γ , PPAR α , CPT1 α , CPT1 β , PGC1 α , UCP1 of BAT from male Park7^{ΔUcp1} and Flox mice housed at TN for 8 weeks and quantification ($n = 3$ mice per group). Statistical significance was assessed by unpaired Student's *t*-test. All results were expressed as means \pm SEM and * $p < 0.05$, ** $p < 0.01$. Student's two-tailed unpaired *T*-test for 2-group comparisons. Source data are provided as a Source Data file.

Protease Inhibitor Cocktail (Beyotime, P1005). Protein concentration was determined using the BCA Protein Assay Kit (Beyotime, P0012). After separating equal amounts of total protein by SDS-PAGE gels, the proteins were transferred to a PVDF membrane (Millipore) and blocked with 5% milk (fatty-acid free) for 1 h at room temperature. Followed primary antibodies: Anti-UCP1 (Abcam, ab10983, 1:1000), anti-Hsc70 (Abcam, ab51052, 1:1000), total OXPHOS Rodent WB Antibody Cocktail (Abcam, ab110413, 1:250), anti-PPAR α /NR1C1 (novus, NB300-537, 1:1000), anti-PPAR γ (CST, 2435, 1:1000), anti-LAMP-2A (Invitrogen, 51-2200, 1:1000), anti-PGC-1 α (novus, NBPI-04676, 1:1000), anti-CPT1 α (novus, NB100-53791, 1:1000), anti-CPT1 β (ABclonal, A6796, 1:1000), anti-Flag (ABclonal, AE005, 1:2000), anti-DJ-1/PARK7 (ABclonal, A19097, 1:1000), anti- β -tubulin (Covin Biotech, CW0098M, 1:2000), anti-HA (Proteintech, 51064-2-AP, 1:2000), anti-V5(CST, 13202, 1:2000), anti-LAMP2a (Abmart, T55518, 1:1000) were incubated with the membranes, which were then washed three times in TBST (Tris-buffered saline containing 0.1% Tween 20) before visualization using the ECL. Western blot images were analyzed for densitometry using ImageJ (National Institutes of Health)⁵⁸.

For immunoprecipitation⁵⁹, cells were lysed in RIPA buffer (50 mmol/L Tris-HCl (pH 7.4), 150 mmol/L NaCl, 1% sodium deoxycholate, 1% Triton-100, plus 0.1% SDS, Beyotime, P0013B) containing complete Protease Inhibitor Cocktail (Beyotime, P1005) and centrifuged at 12,000 g for 10 min at 4 °C. A portion of the supernatant was mixed with 5x loading buffer to serve as the input sample. The remaining lysates were incubated with antibody at 4 °C overnight. Then added the magnetic conjugated beads (Bimake, B23202) at the 2nd day for 2 h. After washing the beads three times in IP buffer, they were boiled with 2x loading buffer for 10 min and then subjected to western blot analysis using the indicated antibodies. The information of all antibodies used is listed in Table S1.

Q-PCR

Total RNA was extracted from cells or homogenized tissues using Trizol reagent (Ambion, 15596018) according to the manufacturer's instructions. The isolated RNA was reverse-transcribed using the cDNA Synthesis Kit (ABI, 4368813), and the resulting cDNA was used for qPCR on a CFX384 real-time PCR detection system (Bio-Rad). The 2⁻(Delta Ct) method with 36b4 as the internal reference control was used to determine the relative mRNA expression level. The primer sequences are listed in Table S2.

Electron microscopy

BAT was cut into 1-mm³ fragments, washed in fresh 0.1 M phosphate buffer (pH 7.4), and fixed in 2.5% (vol/vol) glutaraldehyde overnight at 4 °C (Solarbio, P1126). After three times of wash in fresh 0.1 M phosphate buffer (pH 7.4) for 10 min, tissues were fixed in 1% osmium tetroxide for 1 h on ice and washed three times in 0.1 M phosphate buffer for 10 min. Using en bloc stained with 2% Uranyl acetate on ice overnight, dehydrated in SPON of different gradients. The grids were imaged with a JEM-2100 transmission electron microscope (Hitachi HT7700, Japan).

Histological analysis

Tissues (BAT, iWAT, eWAT, and liver) were fixed with 4% PFA for 24 h. After embedding in paraffin, the tissues were sectioned at 5 μm and stained with hematoxylin and eosin. Immunohistochemistry was performed by rehydrating and boiling the sections in 10 mM citric acid buffer (pH 6.0) at 95 °C for 15 min. Primary antibodies were applied overnight at 4 °C, followed by visualization using goat anti-rabbit HRP-conjugated secondary antibody and the DAB substrate detection kit (ZSGB-BIO, ZLI-9017).

Mitochondria Isolation

Freshly dissected BAT tissue from 8-week-old male mice was homogenized in mitochondria isolation buffer (210 mM Mannitol, 70 mM Sucrose, 1 mM EGTA, 5 mM HEPES pH7.5, 0.5% BSA). The homogenate is filtered through two layers of gauze and centrifuged at 8500 g for 10 min. The hard-packed fat layer and supernatant liquid are discarded by rapidly inverting the tube. The walls of the tube are carefully wiped with a paper tissue to remove adhering fat. The pellet is resuspended in a small volume of mitochondria isolation buffer and transferred to a clean tube. The suspension is centrifuged at 700 g for 10 min. The supernatant is decanted to a fresh tube, and the nuclear pellet is discarded. The supernatant is centrifuged at 8500 g for 10 min⁶⁰. The mitochondrial pellet was resuspended in 25 μl of isolation buffer and protein was quantitated using the BCA assay.

Mass spectrometry

Immunoprecipitation was performed on HEK 293 T cells transfected with Park7-flag using anti-flag antibody. The Phos-tag SDS-PAGE-separated immunoprecipitates and mitochondrial lysis were Coomassie blue-stained. The bands of interest were in-gel digested using sequencing-grade modified trypsin, and the peptides were analyzed by liquid chromatography-tandem mass spectrometry with nano-LC combined with Orbitrap Q Exactive mass spectrometer. The peptides were further verified using the phosphoRS 3.1 node in Proteome Discoverer software.

RNA sequencing

Trizol reagent was used for tissue total RNA extraction according to the manufacturer's protocol. RNA-Seq analysis was performed by the BGI Bio Inc. For RNA-seq analysis, cDNA libraries were constructed with the TruSeq mRNA Library Kit using 1 μg of total RNA. The total RNA was sequenced by the NovaSeq 6000 System (Macrogen). The RNA-seq data were deposited in Gene Expression Omnibus.

Structural analysis based on STRING and AF2

The online search functionality of STRING database version 12.0 was utilized to identify the target protein and species. Various evidence channels were used, encompassing automated text mining of the scientific literature, computational interaction predictions from co-expression, conserved genomic context, databases of interaction experiments and known complexes/pathways from curated sources. The interaction score was computed by combining probabilities from these diverse source types. Interactions that had a confidence level of <50% were excluded from the study. Sequences of Park7,

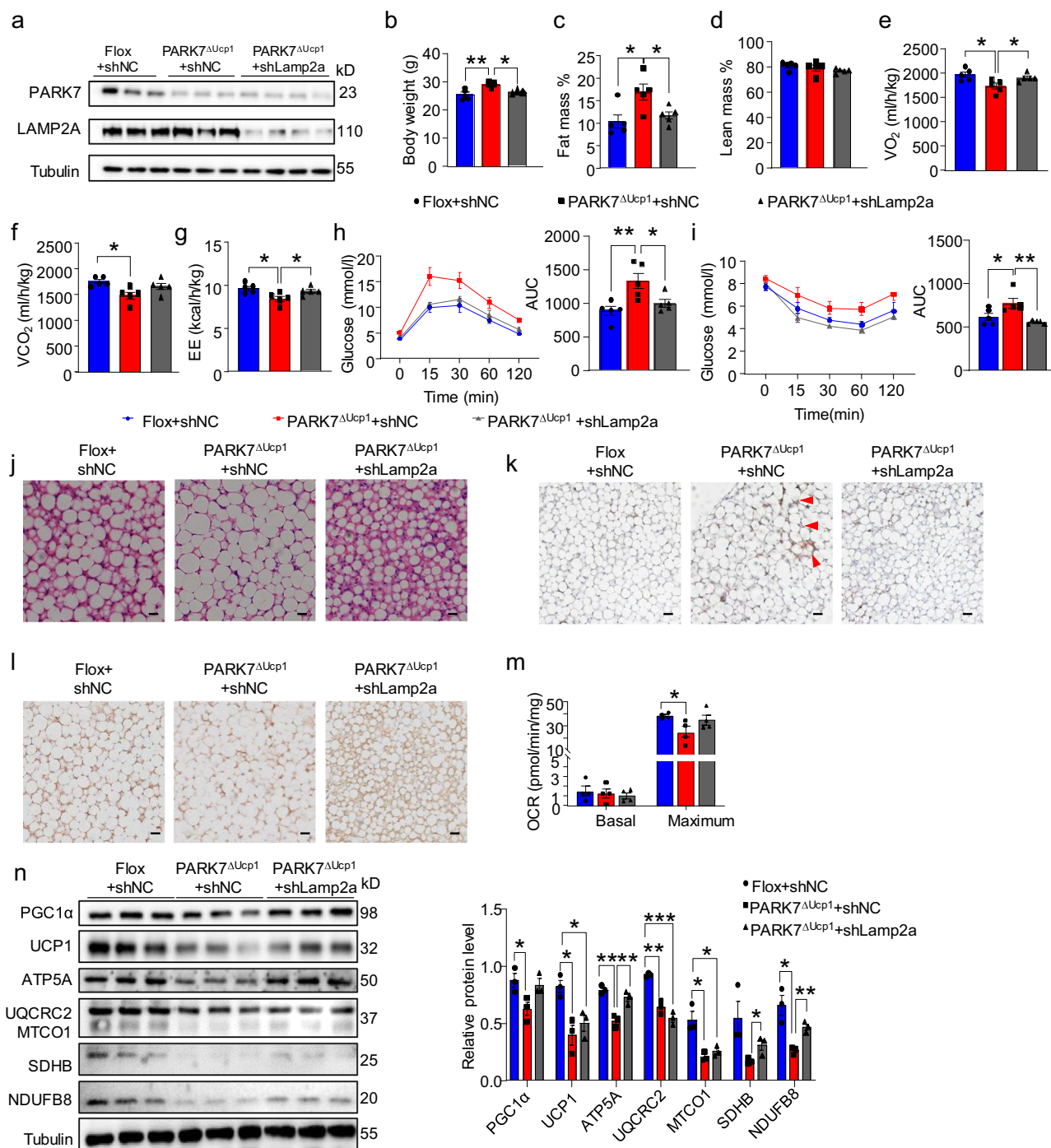


Fig. 7 | CMA activity is required for *Park7* ablation-induced BAT whitening.

a Immunoblotting for PARK7 and LAMP2A protein levels of BAT from male *Park7^{ΔUcp1}* and Flox mice 4 weeks after injection with AAV-shScramble or AAV-shLamp2a and totally housed at TN for 8 weeks. **b–i** Measurements of metabolic parameters of indicated mice housed at TN for 8 weeks, including body weight (**b**), $n = 5$ mice per group; fat mass to body weight ratio (**c**), $n = 5$ mice per group; lean mass to body weight ratio (**d**), $n = 5$ mice per group; quantitation of VO_2 (**e**), $n = 5$ mice per group; quantitation of VCO_2 (**f**), $n = 5$ mice per group; quantitation of EE (**g**), $n = 5$ mice per group; GTT and AUC of GTT (**h**), $n = 5$ mice per group; ITT and

AUC of ITT (**i**), $n = 5$ mice per group. **j–l** Histochemistry analysis, including representative hematoxylin-eosin staining of BAT (**j**), representative immunohistochemical F4/80 (**k**) or UCP1 staining of BAT (**l**). Scale bar, 20 μm . **m** OCR analysis of BAT ($n = 4$). **n** Immunoblotting for PGC1 α , UCP1 and mitochondrial protein levels of BAT and quantification ($n = 3$ mice per group). Statistical significance was assessed by unpaired Student's *t*-test. All results were expressed as means \pm SEM, * $p < 0.05$, ** $p < 0.01$, *** $p < 0.005$. Student's two-tailed unpaired *T*-test for 2-group comparisons. Source data are provided as a Source Data file.

HSC70, and LAMP2A proteins were sourced from UniProt. The AF2-Multimer software was utilized according to guidelines detailed in the document (<https://github.com/deepmind/alphafold>)⁶¹. The analysis of interaction sites and the mutants design based on AF2-predicted complex structures was executed in PyMOL and Chimera. In the instances indicated, predictions of Park7/HSC70 interactions

are colored corresponding to the AlphaFold2-derived per-residue confidence metric known as the local distance difference test (pLDDT). The pLDDT score represents the model's predicted score on the IDDT-Ca metric, with a scale ranging from 0 to 100, where 100 signifies the highest confidence. This score was used to color the models in PyMOL.

Statistical analysis

Data were presented as means \pm SEM and analyzed using Prism 8 (GraphPad) or Microsoft Excel 2019. An unpaired two-tailed Student's *t*-test was used to compare two groups. Significance was set a priori at $p < 0.05$.

Reporting summary

Further information on research design is available in the Nature Portfolio Reporting Summary linked to this article.

Data availability

Data supporting the findings of this study are available in the article and its Supplementary information. Source data are provided as Source Data file and may be obtained from the corresponding authors upon request. RNA-seq dataset has been deposited in the NCBI Gene Expression 728 Omnibus and are accessible through the accession number GSE239793. Source data are provided with this paper.

References

- Kong, X. et al. Brown adipose tissue controls skeletal muscle function via the secretion of myostatin. *Cell Metab.* **28**, 631–643 e633 (2018).
- Cannon, B. & Nedergaard, J. Brown adipose tissue: function and physiological significance. *Physiol. Rev.* **84**, 277–359 (2004).
- Cannon, B., de Jong, J. M. A., Fischer, A. W., Nedergaard, J. & Petrovich, N. Human brown adipose tissue: Classical brown rather than brite/beige? *Exp. Physiol.* **105**, 1191–1200 (2020).
- Fischer, A. W., Cannon, B. & Nedergaard, J. Optimal housing temperatures for mice to mimic the thermal environment of humans: An experimental study. *Mol. Metab.* **7**, 161–170 (2018).
- Fischer, A. W., Cannon, B. & Nedergaard, J. The answer to the question “What is the best housing temperature to translate mouse experiments to humans?” is: thermoneutrality. *Mol. Metab.* **26**, 1–3 (2019).
- Keijer, J., Li, M. & Speakman, J. R. What is the best housing temperature to translate mouse experiments to humans? *Mol. Metab.* **25**, 168–176 (2019).
- Ziqubu, K. et al. An insight into brown/beige adipose tissue whitening, a metabolic complication of obesity with the multifactorial origin. *Front Endocrinol. (Lausanne)* **14**, 1114767 (2023).
- Chouchani, E. T., Kazak, L. & Spiegelman, B. M. New advances in adaptive thermogenesis: UCP1 and beyond. *Cell Metab.* **29**, 27–37 (2019).
- Adamovich, Y. et al. The protein level of PGC-1 α , a key metabolic regulator, is controlled by NADH-NQO1. *Mol. Cell Biol.* **33**, 2603–2613 (2013).
- Finck, B. N. & Kelly, D. P. PGC-1 coactivators: inducible regulators of energy metabolism in health and disease. *J. Clin. Invest.* **116**, 615–622 (2006).
- Kong, X. et al. IRF4 is a key thermogenic transcriptional partner of PGC-1 α . *Cell* **158**, 69–83 (2014).
- Kong, X. et al. Sirtuin 3, a new target of PGC-1 α , plays an important role in the suppression of ROS and mitochondrial biogenesis. *PLoS One* **5**, e11707 (2010).
- Olson, B. L. et al. SCF β acts antagonistically to the PGC-1 α transcriptional coactivator by targeting it for ubiquitin-mediated proteolysis. *Genes Dev.* **22**, 252–264 (2008).
- Trausch-Azar, J., Leone, T. C., Kelly, D. P. & Schwartz, A. L. Ubiquitin proteasome-dependent degradation of the transcriptional coactivator PGC-1 α via the N-terminal pathway. *J. Biol. Chem.* **285**, 40192–40200 (2010).
- Sass, F. et al. TFEB deficiency attenuates mitochondrial degradation upon brown adipose tissue whitening at thermoneutrality. *Mol. Metab.* **47**, 101173 (2021).
- Kaushik, S. & Cuervo, A. M. The coming of age of chaperone-mediated autophagy. *Nat. Rev. Mol. Cell Biol.* **19**, 365–381 (2018).
- Robert, G., Jacquel, A. & Auberger, P. Chaperone-mediated autophagy and its emerging role in hematological malignancies. *Cells* **8**, 1260 (2019).
- Schneider, J. L., Suh, Y. & Cuervo, A. M. Deficient chaperone-mediated autophagy in liver leads to metabolic dysregulation. *Cell Metab.* **20**, 417–432 (2014).
- Kaushik, S. et al. Chaperone-mediated autophagy regulates adipocyte differentiation. *Sci. Adv.* **8**, eabq2733 (2022).
- Bonifati, V. et al. Mutations in the DJ-1 gene associated with autosomal recessive early-onset parkinsonism. *Science* **299**, 256–259 (2003).
- Krebiehl, G. et al. Reduced basal autophagy and impaired mitochondrial dynamics due to loss of Parkinson's disease-associated protein DJ-1. *PLoS One* **5**, e9367 (2010).
- Kim, J. M. et al. DJ-1 contributes to adipogenesis and obesity-induced inflammation. *Sci. Rep.* **4**, 4805 (2014).
- Silvester, A. J., Aseer, K. R. & Yun, J. W. Ablation of DJ-1 impairs brown fat function in diet-induced obese mice. *Biochimie* **154**, 107–118 (2018).
- Inberg, A. & Linial, M. Protection of pancreatic beta-cells from various stress conditions is mediated by DJ-1. *J. Biol. Chem.* **285**, 25686–25698 (2010).
- Jain, D. et al. Age- and diet-dependent requirement of DJ-1 for glucose homeostasis in mice with implications for human type 2 diabetes. *J. Mol. Cell Biol.* **4**, 221–230 (2012).
- Jo, H. S. et al. Tat-DJ-1 inhibits oxidative stress-mediated RINm5F cell death through suppression of NF- κ B and MAPK activation. *Med Chem. Res.* **25**, 2589–2598 (2016).
- Shi, S. Y. et al. DJ-1 links muscle ROS production with metabolic reprogramming and systemic energy homeostasis in mice. *Nat. Commun.* **6**, 7415 (2015).
- Lahiri, V., Hawkins, W. D. & Klionsky, D. J. Watch What You (Self-) Eat: Autophagic Mechanisms that Modulate Metabolism. *Cell Metab.* **29**, 803–826 (2019).
- Kuma, A. et al. The role of autophagy during the early neonatal starvation period. *Nature* **432**, 1032–1036 (2004).
- Wang, L., Klionsky, D. J. & Shen, H. M. The emerging mechanisms and functions of microautophagy. *Nat. Rev. Mol. Cell Biol.* **24**, 186–203 (2023).
- Szklarczyk, D. et al. The STRING database in 2023: protein-protein association networks and functional enrichment analyses for any sequenced genome of interest. *Nucleic Acids Res.* **51**, D638–D646 (2023).
- Roh, H. C. et al. Warming induces significant reprogramming of beige, but not brown, adipocyte cellular identity. *Cell Metab.* **27**, 1121–1137.e1125 (2018).
- Niska-Blakie, J. et al. Knockout of the non-essential gene SUGCT creates diet-linked, age-related microbiome disbalance with a diabetes-like metabolic syndrome phenotype. *Cell Mol. Life Sci.* **77**, 3423–3439 (2020).
- Beaton, N. et al. TUSC5 regulates insulin-mediated adipose tissue glucose uptake by modulation of GLUT4 recycling. *Mol. Metab.* **4**, 795–810 (2015).
- Song, W. et al. Organic cation transporter 3 (Oct3) is a distinct catecholamines clearance route in adipocytes mediating the beiging of white adipose tissue. *PLoS Biol.* **17**, e2006571 (2019).
- Cuervo, A. M. & Dice, J. F. A receptor for the selective uptake and degradation of proteins by lysosomes. *Science* **273**, 501–503 (1996).
- Civelek, M. et al. Genetic regulation of adipose gene expression and cardio-metabolic traits. *Am. J. Hum. Genet.* **100**, 428–443 (2017).
- de Jong, J. M. A. et al. Human brown adipose tissue is phenocopied by classical brown adipose tissue in physiologically humanized mice. *Nat. Metab.* **1**, 830–843 (2019).

39. Zhou, W. et al. Phenylbutyrate up-regulates the DJ-1 protein and protects neurons in cell culture and in animal models of Parkinson disease. *J. Biol. Chem.* **286**, 14941–14951 (2011).
40. Miyazaki, S. et al. DJ-1-binding compounds prevent oxidative stress-induced cell death and movement defect in Parkinson's disease model rats. *J. Neurochem.* **105**, 2418–2434 (2008).
41. Zhang, S. et al. Skeletal muscle-specific DJ-1 ablation-induced atrogenes expression and mitochondrial dysfunction contributing to muscular atrophy. *J. Cachexia Sarcopenia Muscle* **14**, 2126–2142 (2023).
42. Cuervo, A. M., Knecht, E., Terlecky, S. R. & Dice, J. F. Activation of a selective pathway of lysosomal proteolysis in rat liver by prolonged starvation. *Am. J. Physiol.* **269**, C1200–C1208 (1995).
43. Kiffin, R., Christian, C., Knecht, E. & Cuervo, A. M. Activation of chaperone-mediated autophagy during oxidative stress. *Mol. Biol. Cell* **15**, 4829–4840 (2004).
44. Kaushik, S. & Cuervo, A. M. Methods to monitor chaperone-mediated autophagy. *Methods Enzymol.* **452**, 297–324 (2009).
45. Juste, Y. R. & Cuervo, A. M. Analysis of chaperone-mediated autophagy. *Methods Mol. Biol.* **1880**, 703–727 (2019).
46. Rosen, E. D. & Spiegelman, B. M. What we talk about when we talk about fat. *Cell* **156**, 20–44 (2014).
47. Montilla, S. I. et al. Heat stress causes oxidative stress but not inflammatory signaling in porcine skeletal muscle. *Temperature* **1**, 42–50 (2014).
48. Thomas, K. J. et al. DJ-1 acts in parallel to the PINK1/parkin pathway to control mitochondrial function and autophagy. *Hum. Mol. Genet.* **20**, 40–50 (2011).
49. Kaushik, S. & Cuervo, A. M. Chaperone-mediated autophagy: a unique way to enter the lysosome world. *Trends Cell Biol.* **22**, 407–417 (2012).
50. Bandyopadhyay, U., Kaushik, S., Varticovski, L. & Cuervo, A. M. The chaperone-mediated autophagy receptor organizes in dynamic protein complexes at the lysosomal membrane. *Mol. Cell Biol.* **28**, 5747–5763 (2008).
51. Cuervo, A. M. & Dice, J. F. Regulation of lamp2a levels in the lysosomal membrane. *Traffic* **1**, 570–583 (2000).
52. Bandyopadhyay, U., Sridhar, S., Kaushik, S., Kiffin, R. & Cuervo, A. M. Identification of regulators of chaperone-mediated autophagy. *Mol. Cell* **39**, 535–547 (2010).
53. Arias, E. et al. Lysosomal mTORC2/PHLPP1/Akt regulate chaperone-mediated autophagy. *Mol. Cell* **59**, 270–284 (2015).
54. Feldmann, H. M., Golozoubova, V., Cannon, B. & Nedergaard, J. UCP1 ablation induces obesity and abolishes diet-induced thermogenesis in mice exempt from thermal stress by living at thermoneutrality. *Cell Metab.* **9**, 203–209 (2009).
55. Xu, C. Y. et al. DJ-1 inhibits alpha-synuclein aggregation by regulating chaperone-mediated autophagy. *Front. Aging Neurosci.* **9**, 308 (2017).
56. Imberechts, D. et al. DJ-1 is an essential downstream mediator in PINK1/parkin-dependent mitophagy. *Brain* **145**, 4368–4384 (2022).
57. Kirchner, P. et al. Proteome-wide analysis of chaperone-mediated autophagy targeting motifs. *PLoS Biol.* **17**, e3000301 (2019).
58. Gao, H. et al. Kindlin-2 inhibits TNF/NF-kappaB-Caspase 8 pathway in hepatocytes to maintain liver development and function. *Elife* **12**, e81792 (2023).
59. Gao, H. et al. Kindlin-2 haploinsufficiency protects against fatty liver by targeting Foxo1 in mice. *Nat. Commun.* **13**, 1025 (2022).
60. Cannon, B. & Lindberg, O. Mitochondria from brown adipose tissue: isolation and properties. *Methods Enzymol.* **55**, 65–78 (1979).
61. Evans, R. et al. Protein complex prediction with AlphaFold-Multimer. *bioRxiv* <https://doi.org/10.1101/2021.10.04.463034> (2021).

Acknowledgements

The authors acknowledge Dr. Evan Rosen for the suggestions and the assistance of the platform of State Key Laboratory of Genetic Engineering at Fudan University. This work was funded by the National Key R&D Program of China (2023YFA1802000) to H.G., the National Natural Science Foundation of China (92457301, 92157203) to X.K., the National Natural Science Foundation of China (32371194) to H.G., the National Natural Science Foundation of China (32130050) to J.Z. L.

Author contributions

X.K., H.G. and L.J. designed research; Y.Z., X.Z., S.Z., Y.S., Y.C., P.Z., X.L., H.Z. and H.G. performed experiments; H.W., and Y.F., performed bioinformatics and MS analysis. Z.L., P.C., Y.X., H.G., X.K. analyzed data; and X.K. wrote the paper. All authors reviewed and contributed to the manuscript.

Competing interests

The authors declare no competing interest.

Additional information

Supplementary information The online version contains supplementary material available at <https://doi.org/10.1038/s41467-025-59618-0>.

Correspondence and requests for materials should be addressed to Huanqing Gao, Li Jin or Xingxing Kong.

Peer review information *Nature Communications* thanks the anonymous reviewers for their contribution to the peer review of this work. A peer review file is available.

Reprints and permissions information is available at <http://www.nature.com/reprints>

Publisher's note Springer Nature remains neutral with regard to jurisdictional claims in published maps and institutional affiliations.

Open Access This article is licensed under a Creative Commons Attribution-NonCommercial-NoDerivatives 4.0 International License, which permits any non-commercial use, sharing, distribution and reproduction in any medium or format, as long as you give appropriate credit to the original author(s) and the source, provide a link to the Creative Commons licence, and indicate if you modified the licensed material. You do not have permission under this licence to share adapted material derived from this article or parts of it. The images or other third party material in this article are included in the article's Creative Commons licence, unless indicated otherwise in a credit line to the material. If material is not included in the article's Creative Commons licence and your intended use is not permitted by statutory regulation or exceeds the permitted use, you will need to obtain permission directly from the copyright holder. To view a copy of this licence, visit <http://creativecommons.org/licenses/by-nc-nd/4.0/>.

© The Author(s) 2025